

Solar Wind Drivers of Auroral Omega Bands

V. Cribb^{1,2}, T. I. Pulkkinen¹, L. Kepko², B. Gallardo-Lacourt^{2,3}, E. Donovan⁴

¹Department of Climate and Space Sciences and Engineering, University of Michigan, Ann Arbor, MI, USA

²NASA Goddard Space Flight Center, Greenbelt, MD, USA

³Department of Physics, Catholic University of America, Washington, D.C., USA

⁴Department of Physics and Astronomy, University of Calgary, Calgary, Alberta, Canada

Key Points:

- Omega bands are mesoscale structures that emerge as eastward moving wave-like structures at the equatorward border of the auroral oval.
- We perform a superposed epoch analysis of the solar wind parameters measured during 28 omega band events from 2006-2013.
- We find that omega bands are frequently driven by enhanced solar wind density during stream interaction regions.

Corresponding author: Vivian Cribb, vcribb@umich.edu

Abstract

Omega bands are mesoscale auroral structures emerging as eastward moving sinusoidal undulations well within the closed field line region of the auroral oval. While associated with geomagnetic activity, neither specific conditions of their appearance nor their causes are well understood. We perform a superposed epoch analysis of OMNI and SuperMAG measurements taken during 28 omega band events recorded by auroral all-sky imager (ASI) observations from 2006-2013 to identify their solar wind drivers. We find local enhancements in the solar wind flow speed, magnetic field, pressure, and proton density at the onset of the omega band observation. In the magnetosphere-ionosphere, we see enhancements in the ring current, partial ring current, and auroral electrojets. These features are consistent with geomagnetic activity caused by stream interaction regions (SIRs). 19 of our events overlap with SIRs from published event catalogs. Our findings suggest that omega bands are driven by SIR-like events.

Plain Language Summary

Omega bands are eastward moving wave-like structures in the aurora that typically appear at the equatorward border of the auroral oval during periods of enhanced activity in Earth's magnetosphere. However, the specific drivers of these structures are not well understood. In this work, we perform a statistical analysis of spacecraft observations taken from multiple omega band events to identify potential drivers of these structures. We find that the solar wind exhibits increased speed, pressure, and particle density when omega bands appear overhead. These features are consistent with localized compression in the solar wind generated when a fast solar wind stream interacts with a slower leading stream. Our work suggests that the appearance of omega bands is driven by this compression.

1 Introduction

Omega band auroral patterns are mesoscale structures that appear as a result of a solar wind-magnetosphere-ionosphere interaction, and are highly relevant as a diagnostic of magnetic perturbations at Earth resulting in space weather events (Forsyth et al., 2020). Omega bands emerge as sinusoidal undulations well within the closed field line region of the auroral oval (Akasofu, 1974) that are 400-1000 km in scale and drift eastward at 0.4-2 km/s (Opgenoorth et al., 1994). They are typically seen in the post-midnight sector, and are associated with pairs of upward- and downward-aligned field aligned currents (FACs) corresponding to the structures' bright and dark regions, respectively (Opgenoorth et al., 1983; Amm et al., 2005). Pulsating auroras have also been observed in the center of these structures during active periods (Oguti, 1981).

Omega bands appear during periods of geomagnetic activity (e.g. M. G. Henderson, 2012). They have been observed during substorms or following substorm intensification (Pellinen, 1992), but have also been seen during periods of steady magnetospheric convection (Solov'yev et al., 1999). The appearance of omega bands during substorms is not agreed upon. Historically, omega bands have been associated with the substorm recovery phase (Akasofu, 1974; Opgenoorth et al., 1994). However, Partamies et al. (2017) performed a statistical study of the auroral electrojet indices and IMF B_z from 483 omega band events and found that a third of these events occurred during the expansion phase.

The appearance of omega bands is associated with fluctuations in the Earth's magnetic field. Ground magnetometers measure Ps6 pulsations of 4-40 minute periods (Saito, 1978) when omega bands appear overhead. Omega bands are also thought to be the ionospheric mapping of magnetospheric processes that generate rapid time varying magnetic fields, or dB/dt (Schillings et al., 2022). High values of dB/dt cause geomagnetically induced currents (GICs), which can oversaturate transformers (Schrijver et al., 2015) and lead to overvoltages in telecommunication and railway equipment (Pirjola & Boteler, 2002).

Understanding the causes of omega bands may therefore contribute to our ability to understand the ground impacts of space weather.

Although omega bands have been associated with sources in the inner magnetosphere, their exact drivers are not well understood. Magnetic mapping has traced omega bands to regions in the magnetotail located between 5–13 R_E in the near-Earth plasma sheet (e.g. Pulkkinen et al., 1991; Opgenoorth et al., 1994; Andreeva et al., 2021). Several studies have proposed Kelvin-Helmholtz instabilities at varying locations in the plasma sheet as the primary driver of omega bands (e.g. Rostoker & Samson, 1984; Janhunen & Huuskonen, 1993; Wild et al., 2000). Conversely, M. Henderson et al. (2002) suggests that omega bands are driven by fast Earthward flows. Auroral streamers are the ionospheric manifestation of bursty bulk flows (M. G. Henderson et al., 1998; Sergeev et al., 1999, 2000), and they can evolve directly into omega bands.

Among the existing body of literature on omega bands, the solar wind parameters associated with these auroral forms have not been examined in a large statistical study. Previous statistical studies of omega bands (Vokhmyanin et al., 2021; Andreeva et al., 2021; Partamies et al., 2017) focus on ground-based electrodynamic measurements and ionospheric parameters evaluated during omega band events. In-situ magnetospheric data associated with omega bands have been identified (Weygand et al., 2015; Wild et al., 2011), but are limited to case studies of individual events.

Stream interaction regions (SIRs) are known to drive extended intervals of magnetospheric activity (Richardson, 2018). They form when a fast solar wind stream from a coronal hole overtakes a leading slow wind from a streamer, resulting in localized compression in the solar wind and rarefaction behind the leading edge (Gosling & Pizzo, 1999). They are characterized by enhancements in solar wind speed and density and rotation of the IMF. Dynamic pressure fluctuations in the compression region between the two streams, driven primarily by the solar wind number density, have been shown to drive magnetospheric ultra low frequency waves (Kilpua et al., 2013; Kepko & Viall, 2019). In combination with enhanced southward IMF, SIRs can lead to High Intensity Long Duration Continuous AE Activity (HILDCAA) events (Tsurutani & Gonzalez, 1987) that may be conducive to omega band formation.

In this work, we perform a superposed epoch analysis of the solar wind parameters measured during 28 omega band events from 2006–2013 and find that our results are consistent with the characteristics of SIRs. Section 2 describes the data used for this analysis and Section 3 describes the results obtained.

2 Data

The events selected for this statistical analysis have been identified optically using the THEMIS all-sky imager (ASI) array (Mende et al., 2009). THEMIS ASI is based in North America and consists of 21 all-sky cameras, which extend from about 50 to 70 degrees latitude and 200 to 300 degrees longitude in geographic coordinates. These cameras are white light CCD imagers which provide about an hour of local time coverage, with a field-of-view of ~ 600 km (Donovan et al., 2006). To formulate our event list for the superposed epoch analysis, we used keograms—north-south slices obtained from the THEMIS ASI stations—from 2006 to 2013.

We visually identified 28 events from 2006 to 2013 where at least one clear protrusion emerged from the equatorward oval and drifted eastward. Events were chosen on the basis of their visual resemblance to (1) wave-like forms in the edge of the oval or (2) torches separated by dark regions, where torches refer to luminous poleward protrusions in the auroral oval (Akasofu & Kimball, 1964; M. Henderson et al., 2002). The onset time of each event was recorded as the minute when the first protrusion appeared in the field of view of the ASI camera, while the end time was defined as the minute when the last

protrusion exited the camera's field of view. The onset time for all events occurred between 23 and 5 MLT. 26 of the 28 onset times occurred post-midnight. On average, the events were 20 minutes in duration.

We examined the solar wind, magnetospheric, and ionospheric parameters from each event. Solar wind data were extracted from the OMNI database and the electrojet indices were measured by SuperMAG ground stations (Gjerloev, 2012). We compared our omega band event list to the SIR catalog identified by Grandin et al. (2019) to identify solar wind structures that coincided with our omega band observations.

The solar wind and magnetospheric data from an omega band event that coincides with an SIR is shown in Fig. 1. This event was observed by the ASI camera at Athabasca on 2006-08-07. The event consists of an omega band which entered the field of view of the ASI camera at 08:43 UT, coinciding with an SIR event that began on 2006-08-07 at 0 UT and ended on 2006-08-10 at 7 UT. The epoch time in Fig. 1 is defined as 08:43 UT on 2006-08-07 and is indicated by a vertical line. 1-minute resolution measurements of IMF B_y , IMF B_z , solar wind flow speed, solar wind density, SYM-H, ASY-H, SMU, and SML are shown for the two week period centered on the epoch time.

At the epoch time, IMF B_y and B_z were enhanced. The solar wind flow speed increased to 600 km/s, while the proton density increased sharply to 40 1/cc two hours before the omega band appeared. The sharp enhancements in speed and density are consistent with a localized compression in the solar wind appearing at the leading edge of an SIR structure.

SYM-H and ASY-H were similarly enhanced at the epoch time. The magnitude of SYM-H peaked one hour before the observation time and reached 70 nT, while ASY-H peaked 45 minutes after observation and reached 100 nT. Activity in SYM-H was sustained for multiple days following the epoch time, which is consistent with SIR-associated substorms.

In the ionosphere, the strength of the upper (SMU) and lower (SML) auroral electrojets (AE) began increasing one day before the omega band observation and peaked sharply one hour after the observation time. We also observed sustained activity in the SML index reaching about -500 nT for multiple days after the epoch time. The prolonged SML activity may be a product of an SIR occurring during a period of enhanced southward IMF, leading to a HILDCAA event.

3 Results

We performed a superposed epoch analysis of the solar wind and magnetospheric measurements taken during all 28 events. 1-minute solar wind, ring current, and partial ring current measurements were obtained from the NASA OMNI dataset. 1-minute upper and lower electrojet indices and local ring current data were taken by SuperMAG ground stations. The superposed epoch analysis was run over the two week period centered on the onset time of each event using SpacePy (Niehof et al., 2022). For this analysis, time was not scaled.

The results of the superposed epoch analysis of the solar wind parameters are shown in Fig. 2, where the epoch time is defined as the onset time for each event. The IMF magnitude begins to increase one day before the epoch time, reaching a local maximum of ~ 10 nT at the time of observation and decreasing to ~ 5 nT over the following day. The IMF also undergoes rotation as the magnitude of IMF B_y is enhanced by ~ 3 nT prior to the time of observation, while IMF B_z reaches a local minimum of -5 nT at the epoch time. Interestingly, while IMF B_y begins to increase three days before the epoch time, the enhancement of IMF B_z only begins over two days later.

The solar wind flow speed increases by ~ 100 km/s in the day surrounding the epoch time. V_y increases and changes sign over the same time interval. The solar wind particle density increases with the flow speed before reaching a maximum of ~ 10 1/cc at the epoch time and dropping to 5 1/cc over the following day.

The same analysis of the magnetospheric parameters are shown in Fig. 3. The magnitude of SYM-H peaks at 25 nT one hour after the epoch time, indicating that the observation time falls during the onset phase of a substorm. Activity in SYM-H continues for multiple days afterwards. SML begins to decrease six hours before the epoch time and reaches a local minimum of -500 nT around one hour after the epoch time, while SMU reaches a local maximum less than an hour later.

The magnitude of ASY-H peaks at 50 nT two hours after the epoch time, indicating an asymmetric ring current. This is also seen in the local time SMR indices, which correlate to midnight (SMR00), dawn (SMR06), noon (SMR12), and dusk (SMR18). All four indices start to decrease six hours before the epoch time. However, SMR00, SMR12, and SMR18 peak one hour after the epoch time, while the SMR index in the dawn sector (SMR06) continues to decrease until six hours after the epoch time. SMR06 is also about half the magnitude of the other indices during this time interval, suggesting a suppression of the dawnside ring current.

4 Discussion

These solar wind observations from our omega band events are consistent with local compression in the solar wind associated with SIR events. The increase in flow speed is associated with a fast solar wind stream overtaking a leading slow stream. The rotation in IMF and increase in proton density are indicative of the resulting compression of the solar wind plasma and magnetic field. A spiral-shaped interaction region forms between the two streams, where the pressure is maximized. This causes the solar wind to be deflected to the west (+y) ahead of the interaction region and to the east (-y) behind the region, which is reflected in the sign change of V_y .

As seen in Fig. 2, the proton density begins increasing about one day before the epoch time and peaks four hours before the omega bands are observed. Using the proton density of the solar wind as a proxy for dynamic pressure, this is consistent with the findings of McPherron et al. (2009), who concluded that the dynamic pressure of the solar wind is expected to begin increasing one day before an SIR stream interface passes Earth. These authors define a stream interface as the point at which the solar wind azimuthal flow angle crosses zero. The initial increase of dynamic pressure (proton density) corresponds to the leading edge of the SIR, while the peak corresponds to the stream interface. This suggests that the stream interface passes Earth shortly before the epoch time.

The interface is followed by a fast stream which carries large amplitude Alfvén waves. These Alfvén waves can rotate the IMF southward, which is reflected in the enhancement of IMF B_z in Fig. 2. Negative IMF B_z drives convection, causing the closure of field-aligned currents in the ionosphere. The resulting Hall currents drive activity in the AE indices, which is seen in the enhancement of SMU and SML in Fig. 3. Geomagnetic activity is also expected to increase after the stream interface, which is reflected in the delayed peak in ASY-H and prolonged activity in SYM-H.

We find that 19 of our 28 omega band events occurred during SIR events listed in the catalog published by Grandin et al. (2019). We performed separate superposed epoch analyses for these 19 events and the remaining 9 events to compare the mean solar wind and magnetospheric parameters between the two groups. The results are shown in Fig. 4. Both types of events feature enhancements in IMF B_y and IMF B_z at the epoch time, with prolonged southward IMF B_z beginning about twelve hours before time zero. In

the SIR events, the solar wind flow speed begins to increase multiple days before the epoch time, reaching a maximum of 600 km/s 24 hours after the observation. In the non-SIR events, the flow speed increases slightly for the six hour period before the epoch time, but does not continue to increase after the observation.

The pressure and proton density of the solar wind for both SIR and non-SIR events peak at the epoch time. The pressure and density for the SIR events begin to increase multiple days before the non-SIR events. Notably, the pressure and density peak at similar values for both classes of events. An initial enhancement is seen in the SML index twelve hours before the epoch time and reaches a peak at the time of omega band observation. The value of SML for the SIR and non-SIR events is similar throughout the two week interval shown in Fig. 4, aside from the two days following the epoch time, when the SIR events appear to exhibit sustained activity in the index.

The similarity in IMF B_z and the SML index at the epoch time for both types of events indicates that activity in the AE is more likely to be driven by enhanced southward IMF and solar wind density, which have similar values at the epoch time, rather than the solar wind flow speed. This suggests that omega bands are associated with geomagnetic activity featuring localized compression and increased density that is characteristic of SIR events, but doesn't necessarily require enhanced flow speed, such as coronal mass ejections (CMEs).

We note that 1 of the 9 non-SIR omega band events occurred within three days of the start time of an SIR event listed in the catalog. In their catalog, Grandin et al. (2019) eliminate multiple candidates for SIR events within the same three day period by retaining the one with the lowest initial solar wind speed. It is possible that this omega band event occurred during an SIR event with a higher initial solar wind speed than the corresponding event in the catalog, and was therefore excluded. The non-SIR events also show a small enhancement in flow speed starting from a relatively low value of ~ 300 km/s at the time of observation. Along with the other parameters, this might be indicative of weak SIRs or CMEs, as discussed above.

5 Conclusions

In this paper, we performed a superposed epoch analysis of solar wind data from 28 omega band events recorded by THEMIS ASI. Our analysis shows that the epoch time is associated with enhanced southward IMF B_z and increased solar wind density and pressure. The epoch time coincides with a substantial peak in AL and a few tens of nT signature in SMR, indicative of strong auroral currents and a weaker, highly asymmetric ring current.

The results of our superposed epoch analysis indicate that omega bands are frequently driven by geomagnetic activity associated with strong increases in the solar wind density. This driving could occur as a result of multiple mechanisms: (1) The localized compression of the solar wind may cause oscillations in the solar wind density. These density oscillations can alter the size of the magnetospheric cavity, driving fluctuations in the magnetospheric field that propagate inward to geosynchronous orbit (Viall et al., 2021). (2) The pressure gradient generated by the enhanced solar wind density drives pulses in tail reconnection, which result in fast flows in the plasma sheet (Forsyth et al., 2020). Omega bands are then formed in the oval by the mechanisms described in M. Henderson et al. (2002).

Based on our ionospheric observations alone, it is not possible to distinguish between these processes, and thus identification of the magnetospheric processes leading to the generation of the characteristic auroral form is left as a future study. However, the behavior of the solar wind and IMF around omega band events clearly point to the significance of negative IMF B_z and persistent high solar wind density, which have not

been reported earlier. Enhanced solar wind density penetrates into the inner magnetosphere over a time scale of many hours (Lee & Roederer, 1982). This enhanced particle density drives magnetospheric compression and enhancements in the density of the inner magnetosphere that may lead to omega band formation.

While earlier works have associated omega bands with the substorm recovery phase, our events occur near or even before the peak in geomagnetic activity. This result agrees with the findings of Partamies et al. (2017), who used a large set of omega band events to conclude that a third of these events occur during the expansion phase.

Finally, while Partamies et al. (2017) use a dataset of 438 omega band events for their analysis, the number of events used for our statistical analysis is limited by the geographic extent and availability of THEMIS ASI cameras. We have also visually identified the events used here, so it is possible that we have selected events of higher intensity that are more likely to be correlated with SIRs.

6 Open Research

The analysis in this paper uses data from THEMIS ASI, OMNI, and SuperMAG. THEMIS ASI data is available at <https://data-portal.phys.ucalgary.ca/>. OMNI data is available through CDAWeb at <https://cdaweb.gsfc.nasa.gov/index.html> and was accessed on January 25, 2024. SuperMAG data is available at <https://supermag.jhuapl.edu/indices/>. The event list is included as supporting information (S1).

Acknowledgments

V. Cribb was supported by NASA grant 80NSSC23K1317 and the Goddard Space Flight Center Internal Scientist Funding Model (competitive work package) program. T. Pulkkinen was supported by NASA grant 80NSSC23K1317. L. Kepko and B. Gallardo-Lacourt were supported by the Goddard Space Flight Center Internal Scientist Funding Model (competitive work package) program. We gratefully acknowledge the SuperMAG collaborators (<https://supermag.jhuapl.edu/info/?page=acknowledgement>) for the SMU and SML indices (Newell & Gjerloev, 2011). We thank Steve Morley for the SpacePy library (Niehof et al., 2022) used in the superposed epoch analysis. We acknowledge NASA CDAWeb for providing access to OMNI data.

References

- Akasofu, S. I. (1974, November). A study of auroral displays photographed from the DMSP-2 satellite and from the Alaska meridian chain of stations. *Space Sci Rev*, 16(5), 617–725. Retrieved 2023-10-04, from <https://doi.org/10.1007/BF00182598> doi: 10.1007/BF00182598
- Akasofu, S. I., & Kimball, D. S. (1964, February). The dynamics of the aurora—I: Instabilities of the aurora. *Journal of Atmospheric and Terrestrial Physics*, 26(2), 205–211. Retrieved 2024-03-27, from <https://www.sciencedirect.com/science/article/pii/0021916964901473> doi: 10.1016/0021-9169(64)90147-3
- Amm, O., Aksnes, A., Stadsnes, J., Østgaard, N., Vondrak, R. R., Germany, G. A., ... Viljanen, A. (2005, February). Mesoscale ionospheric electrodynamics of omega bands determined from ground-based electromagnetic and satellite optical observations. *Annales Geophysicae*, 23(2), 325–342. Retrieved 2023-09-06, from <https://angeo.copernicus.org/articles/23/325/2005/angeo-23-325-2005.html> (Publisher: Copernicus GmbH) doi: 10.5194/angeo-23-325-2005
- Andreeva, V. A., Apatenkov, S. V., Gordeev, E. I., Partamies, N., & Kauristie, K. (2021). Omega Band Magnetospheric Source Location: A

- Statistical Model-Based Study. *Journal of Geophysical Research: Space Physics*, 126(6), e2020JA028997. Retrieved 2023-09-06, from <https://onlinelibrary.wiley.com/doi/abs/10.1029/2020JA028997> (_eprint: <https://onlinelibrary.wiley.com/doi/pdf/10.1029/2020JA028997>) doi: 10.1029/2020JA028997
- Donovan, E., Mende, S., Jackel, B., Frey, H., Syrjäsuo, M., Voronkov, I., ... Connors, M. (2006, September). The THEMIS all-sky imaging array—system design and initial results from the prototype imager. *Journal of Atmospheric and Solar-Terrestrial Physics*, 68(13), 1472–1487. Retrieved 2024-02-12, from <https://www.sciencedirect.com/science/article/pii/S1364682606001118> doi: 10.1016/j.jastp.2005.03.027
- Forsyth, C., Sergeev, V. A., Henderson, M. G., Nishimura, Y., & Gallardo-Lacourt, B. (2020, April). Physical Processes of Meso-Scale, Dynamic Auroral Forms. *Space Sci Rev*, 216(4), 46. Retrieved 2023-10-04, from <https://doi.org/10.1007/s11214-020-00665-y> doi: 10.1007/s11214-020-00665-y
- Gjerloev, J. W. (2012). The SuperMAG data processing technique. *Journal of Geophysical Research: Space Physics*, 117(A9). Retrieved 2023-10-04, from <https://onlinelibrary.wiley.com/doi/abs/10.1029/2012JA017683> (_eprint: <https://onlinelibrary.wiley.com/doi/pdf/10.1029/2012JA017683>) doi: 10.1029/2012JA017683
- Gosling, J., & Pizzo, V. (1999, July). Formation and Evolution of Corotating Interaction Regions and their Three Dimensional Structure. *Space Science Reviews*, 89(1), 21–52. Retrieved 2024-02-12, from <https://doi.org/10.1023/A:1005291711900> doi: 10.1023/A:1005291711900
- Grandin, M., Aikio, A. T., & Kozlovsky, A. (2019). Properties and Geoeffectiveness of Solar Wind High-Speed Streams and Stream Interaction Regions During Solar Cycles 23 and 24. *Journal of Geophysical Research: Space Physics*, 124(6), 3871–3892. Retrieved 2024-02-12, from <https://onlinelibrary.wiley.com/doi/abs/10.1029/2018JA026396> (_eprint: <https://onlinelibrary.wiley.com/doi/pdf/10.1029/2018JA026396>) doi: 10.1029/2018JA026396
- Henderson, M., Kepko, L., Spence, H., Connors, M., Sigwarth, J., Frank, L., ... Yumoto, K. (2002, 03). The evolution of north-south aligned auroral forms into auroral torch structures : The generation of omega bands and ps6 pulsations via flow bursts. In R. M. Winglee (Ed.), *Proceedings of the sixth international conference on substorms* (p. 169-174). Seattle, Washington. doi: 10.13140/RG.2.1.4976.9688
- Henderson, M. G. (2012). Auroral substorms, poleward boundary activations, auroral streamers, omega bands, and onset precursor activity. In *Auroral phenomenology and magnetospheric processes: Earth and other planets* (p. 39-54). American Geophysical Union (AGU). Retrieved from <https://agupubs.onlinelibrary.wiley.com/doi/abs/10.1029/2011GM001165> doi: <https://doi.org/10.1029/2011GM001165>
- Henderson, M. G., Reeves, G. D., & Murphree, J. S. (1998). Are north-south aligned auroral structures an ionospheric manifestation of bursty bulk flows? *Geophysical Research Letters*, 25(19), 3737–3740. Retrieved from <https://agupubs.onlinelibrary.wiley.com/doi/abs/10.1029/98GL02692> doi: <https://doi.org/10.1029/98GL02692>
- Janhunen, P., & Huuskonen, A. (1993). A numerical ionosphere-magnetosphere coupling model with variable conductivities. *Journal of Geophysical Research: Space Physics*, 98(A6), 9519–9530. Retrieved 2023-10-04, from <https://onlinelibrary.wiley.com/doi/abs/10.1029/92JA02973> (_eprint: <https://onlinelibrary.wiley.com/doi/pdf/10.1029/92JA02973>) doi: 10.1029/92JA02973
- Kepko, L., & Viall, N. M. (2019). The Source, Significance, and Mag-

- netospheric Impact of Periodic Density Structures Within Stream Interaction Regions. *Journal of Geophysical Research: Space Physics*, 124(10), 7722–7743. Retrieved 2024-02-12, from <https://onlinelibrary.wiley.com/doi/abs/10.1029/2019JA026962> (_eprint: <https://onlinelibrary.wiley.com/doi/pdf/10.1029/2019JA026962>) doi: 10.1029/2019JA026962
- Kilpua, E. K. J., Hietala, H., Koskinen, H. E. J., Fontaine, D., & Turc, L. (2013, September). Magnetic field and dynamic pressure ULF fluctuations in coronal-mass-ejection-driven sheath regions. *Annales Geophysicae*, 31(9), 1559–1567. Retrieved 2024-02-12, from <https://angeo.copernicus.org/articles/31/1559/2013/> (Publisher: Copernicus GmbH) doi: 10.5194/angeo-31-1559-2013
- Lee, L. C., & Roederer, J. G. (1982). Solar wind energy transfer through the magnetopause of an open magnetosphere. *Journal of Geophysical Research: Space Physics*, 87(A3), 1439–1444. Retrieved 2024-03-14, from <https://onlinelibrary.wiley.com/doi/abs/10.1029/JA087iA03p01439> (_eprint: <https://onlinelibrary.wiley.com/doi/pdf/10.1029/JA087iA03p01439>) doi: 10.1029/JA087iA03p01439
- McPherron, R. L., Kepko, L., Pulkkinen, T. I., Hsu, T. S., Weygand, J. W., & Bargatze, L. F. (2009, August). Changes in the response of the AL Index with solar cycle and epoch within a corotating interaction region. *Annales Geophysicae*, 27(8), 3165–3178. Retrieved 2024-02-12, from <https://angeo.copernicus.org/articles/27/3165/2009/> (Publisher: Copernicus GmbH) doi: 10.5194/angeo-27-3165-2009
- Mende, S. B., Harris, S. E., Frey, H. U., Angelopoulos, V., Russell, C. T., Donovan, E., ... Petricolas, L. M. (2009). The THEMIS Array of Ground-based Observatories for the Study of Auroral Substorms. In J. L. Burch & V. Angelopoulos (Eds.), *The THEMIS Mission* (pp. 357–387). New York, NY: Springer. Retrieved 2024-03-27, from https://doi.org/10.1007/978-0-387-89820-9_16 doi: 10.1007/978-0-387-89820-9_16
- Newell, P. T., & Gjerloev, J. W. (2011). Substorm and magnetosphere characteristic scales inferred from the SuperMAG auroral electrojet indices. *Journal of Geophysical Research: Space Physics*, 116(A12). Retrieved 2024-03-28, from <https://onlinelibrary.wiley.com/doi/abs/10.1029/2011JA016936> (_eprint: <https://onlinelibrary.wiley.com/doi/pdf/10.1029/2011JA016936>) doi: 10.1029/2011JA016936
- Niehof, J. T., Morley, S. K., Welling, D. T., & Larsen, B. A. (2022). The spacepy space science package at 12 years. *Frontiers in Astronomy and Space Sciences*, 9. doi: 10.3389/fspas.2022.1023612
- Oguti, T. (1981). Tv Observations of Auroral Arcs. In *Physics of Auroral Arc Formation* (pp. 31–41). American Geophysical Union (AGU). Retrieved 2024-02-12, from <https://onlinelibrary.wiley.com/doi/abs/10.1029/GM025p0031> (_eprint: <https://onlinelibrary.wiley.com/doi/pdf/10.1029/GM025p0031>) doi: 10.1029/GM025p0031
- Opgenoorth, H. J., Oksman, J., Kaila, K. U., Nielsen, E., & Baumjohann, W. (1983). Characteristics of eastward drifting omega bands in the morning sector of the auroral oval. *Journal of Geophysical Research: Space Physics*, 88(A11), 9171–9185. Retrieved 2024-02-12, from <https://onlinelibrary.wiley.com/doi/abs/10.1029/JA088iA11p09171> (_eprint: <https://onlinelibrary.wiley.com/doi/pdf/10.1029/JA088iA11p09171>) doi: 10.1029/JA088iA11p09171
- Opgenoorth, H. J., Persson, M. a. L., Pulkkinen, T. I., & Pellinen, R. J. (1994). Recovery phase of magnetospheric substorms and its association with morning-sector aurora. *Journal of Geophysical Research: Space Physics*, 99(A3), 4115–4129. Retrieved 2023-10-04, from <https://>

- onlinelibrary.wiley.com/doi/abs/10.1029/93JA01502 (_eprint:
https://onlinelibrary.wiley.com/doi/pdf/10.1029/93JA01502) doi: 10.1029/
93JA01502
- Partamies, N., Weygand, J. M., & Juusola, L. (2017, September). Statistical study
of auroral omega bands. *Annales Geophysicae*, 35(5), 1069–1083. Retrieved
2023-09-06, from [https://angeo.copernicus.org/articles/35/1069/
2017/angeo-35-1069-2017.html](https://angeo.copernicus.org/articles/35/1069/2017/angeo-35-1069-2017.html) (Publisher: Copernicus GmbH) doi:
10.5194/angeo-35-1069-2017
- Pellinen, R. J. (1992). Substorm recovery phase : relationship to next activation.
Proceedings of the International Conference on Substorms(ICS-1), Kiruna,
Sweden, March 1992, 335, 469-475. Retrieved from [https://cir.nii.ac.jp/
crid/1571135649080168960](https://cir.nii.ac.jp/crid/1571135649080168960)
- Pirjola, R., & Boteler, D. (2002). Calculation methods of the electric and
magnetic fields at the Earth's surface produced by a line current. *Radio
Science*, 37(3), 14–1–14–9. Retrieved 2023-10-04, from [https://
onlinelibrary.wiley.com/doi/abs/10.1029/2001RS002576](https://onlinelibrary.wiley.com/doi/abs/10.1029/2001RS002576) (_eprint:
<https://onlinelibrary.wiley.com/doi/pdf/10.1029/2001RS002576>) doi:
10.1029/2001RS002576
- Pulkkinen, T. I., Pellinen, R. J., Koskinen, H. E. J., Opgenoorth, H. J., Murphree,
J. S., Petrov, V., ... Friis-Christensen, E. (1991). Auroral Signatures of
Substorm Recovery Phase: A Case Study. In *Magnetospheric Substorms*
(pp. 333–341). American Geophysical Union (AGU). Retrieved 2024-02-12,
from <https://onlinelibrary.wiley.com/doi/abs/10.1029/GM064p0333>
(_eprint: <https://onlinelibrary.wiley.com/doi/pdf/10.1029/GM064p0333>) doi:
10.1029/GM064p0333
- Richardson, I. G. (2018, January). Solar wind stream interaction regions
throughout the heliosphere. *Living Rev Sol Phys*, 15(1), 1. Retrieved
2024-03-08, from <https://doi.org/10.1007/s41116-017-0011-z> doi:
10.1007/s41116-017-0011-z
- Rostoker, G., & Samson, J. (1984). Can substorm expansive phase effects
and low frequency Pc magnetic pulsations be attributed to the same
source mechanism? *Geophysical Research Letters*, 11(3), 271–274. doi:
10.1029/GL011i003p00271
- Saito, T. (1978). Long-period irregular magnetic pulsation, Pi3. *Space Science Re-
views*, 21(4), 427–467. doi: 10.1007/BF00173068
- Schillings, A., Palin, L., Opgenoorth, H. J., Hamrin, M., Rosenqvist, L., Gjer-
loev, J. W., ... Barnes, R. (2022). Distribution and Occurrence Fre-
quency of dB/dt Spikes During Magnetic Storms 1980–2020. *Space
Weather*, 20(5), e2021SW002953. Retrieved 2023-10-04, from [https://
onlinelibrary.wiley.com/doi/abs/10.1029/2021SW002953](https://onlinelibrary.wiley.com/doi/abs/10.1029/2021SW002953) (_eprint:
<https://onlinelibrary.wiley.com/doi/pdf/10.1029/2021SW002953>) doi:
10.1029/2021SW002953
- Schrijver, C. J., Kauristie, K., Aylward, A. D., Denardini, C. M., Gibson, S. E.,
Glover, A., ... Vilmer, N. (2015, June). Understanding space weather to
shield society: A global road map for 2015–2025 commissioned by COSPAR
and ILWS. *Advances in Space Research*, 55(12), 2745–2807. Retrieved
2023-10-04, from [https://www.sciencedirect.com/science/article/pii/
S0273117715002252](https://www.sciencedirect.com/science/article/pii/S0273117715002252) doi: 10.1016/j.asr.2015.03.023
- Sergeev, V. A., Liou, K., Meng, C. I., Newell, P. T., Brittnacher, M., Parks, G.,
& Reeves, G. D. (1999). Development of auroral streamers in associa-
tion with localized impulsive injections to the inner magnetotail. *Geo-
physical Research Letters*, 26(3), 417-420. Retrieved from [https://
agupubs.onlinelibrary.wiley.com/doi/abs/10.1029/1998GL900311](https://agupubs.onlinelibrary.wiley.com/doi/abs/10.1029/1998GL900311) doi:
<https://doi.org/10.1029/1998GL900311>
- Sergeev, V. A., Sauvaud, J. A., Popescu, D., Kovrazhkin, R. A., Liou, K.,

- Newell, P. T., ... Reeves, G. D. (2000). Multiple-spacecraft observation of a narrow transient plasma jet in the earth's plasma sheet. *Geophysical Research Letters*, 27(6), 851-854. Retrieved from <https://agupubs.onlinelibrary.wiley.com/doi/abs/10.1029/1999GL010729> doi: <https://doi.org/10.1029/1999GL010729>
- Solov'ev, S. I., Baishev, D. G., Barkova, E. S., Engebretson, M. J., Posch, J. L., Hughes, W. J., ... Pilipenko, V. A. (1999). Structure of disturbances in the dayside and nightside ionosphere during periods of negative interplanetary magnetic field Bz. *Journal of Geophysical Research: Space Physics*, 104(A12), 28019-28039. Retrieved 2024-03-28, from <https://onlinelibrary.wiley.com/doi/abs/10.1029/1999JA900286> (_eprint: <https://onlinelibrary.wiley.com/doi/pdf/10.1029/1999JA900286>) doi: 10.1029/1999JA900286
- Tsurutani, B. T., & Gonzalez, W. D. (1987, April). The cause of high-intensity long-duration continuous AE activity (HILDCAAs): Interplanetary Alfvén wave trains. *Planetary and Space Science*, 35(4), 405-412. Retrieved 2024-02-12, from <https://www.sciencedirect.com/science/article/pii/0032063387900973> doi: 10.1016/0032-0633(87)90097-3
- Viall, N. M., DeForest, C. E., & Kepko, L. (2021, August). Mesoscale Structure in the Solar Wind. *Front. Astron. Space Sci.*, 8. Retrieved 2024-03-29, from <https://www.frontiersin.org/articles/10.3389/fspas.2021.735034> (Publisher: Frontiers) doi: 10.3389/fspas.2021.735034
- Vokhmyanin, M., Apatenkov, S., Gordeev, E., Andreeva, V., Partamies, N., Kauristie, K., & Juusola, L. (2021). Statistics on Omega Band Properties and Related Geomagnetic Variations. *Journal of Geophysical Research: Space Physics*, 126(7), e2021JA029468. Retrieved 2023-09-06, from <https://onlinelibrary.wiley.com/doi/abs/10.1029/2021JA029468> (_eprint: <https://onlinelibrary.wiley.com/doi/pdf/10.1029/2021JA029468>) doi: 10.1029/2021JA029468
- Weygand, J., Kivelson, M., Frey, H., Rodriguez, J., Angelopoulos, V., Redmon, R., ... Amm, O. (2015, October). An interpretation of spacecraft and ground based observations of multiple omega band events. *Journal of Atmospheric and Solar-Terrestrial Physics*, 133, 185-204. Retrieved 2023-09-06, from <https://linkinghub.elsevier.com/retrieve/pii/S1364682615300407> doi: 10.1016/j.jastp.2015.08.014
- Wild, J. A., Woodfield, E. E., Donovan, E., Fear, R. C., Grocott, A., Lester, M., ... Björnsson, G. (2011). Midnight sector observations of auroral omega bands. *Journal of Geophysical Research: Space Physics*, 116(A5). Retrieved 2023-09-06, from <https://onlinelibrary.wiley.com/doi/abs/10.1029/2010JA015874> (_eprint: <https://onlinelibrary.wiley.com/doi/pdf/10.1029/2010JA015874>) doi: 10.1029/2010JA015874
- Wild, J. A., Yeoman, T. K., Eglitis, P., & Opgenoorth, H. J. (2000, January). Multi-instrument observations of the electric and magnetic field structure of omega bands. *Annales Geophysicae*, 18(1), 99-110. Retrieved 2024-02-12, from <https://angeo.copernicus.org/articles/18/99/2000/> (Publisher: Copernicus GmbH) doi: 10.1007/s00585-000-0099-6

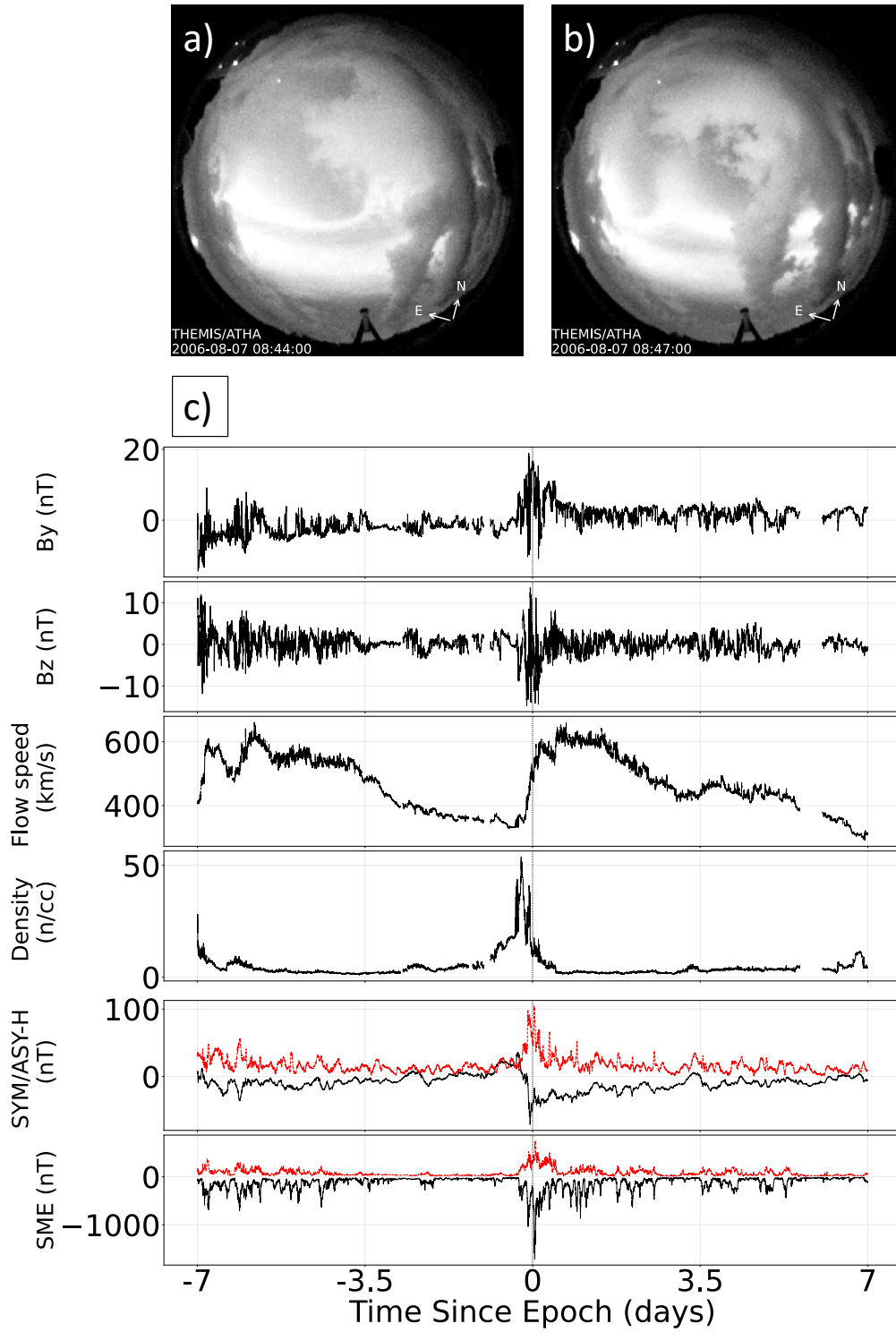


Figure 1. (a) Image taken of omega bands over Athabasca on 2006-08-07 at 08:44 UT. (b) Image taken of an omega band over Athabasca on the same day at 08:47 UT. (c) Summary plot of this omega band event. The epoch is the minute when the omega band enters the camera's field of view. B_y and B_z are plotted in GSM coordinates. At time zero, we see fluctuations in IMF and enhancements in solar wind flow speed, solar wind density, SYM-H (black), ASY-H (red), SMU (red), and SML (black).

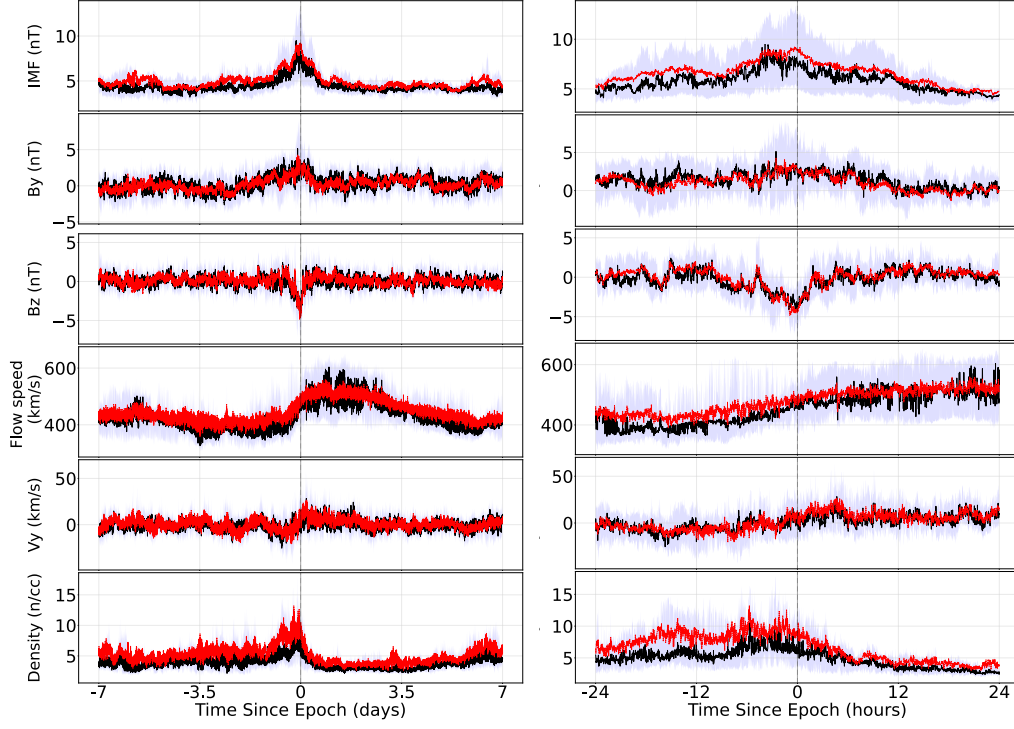


Figure 2. Two week (left) and two day (right) superposed epoch analyses of IMF magnitude, IMF B_y , IMF B_z , solar wind flow speed, solar wind V_y , and solar wind proton density measured in GSM coordinates during the 28 omega band events. The epoch time is defined as the minute that the omega bands were observed. The mean value of each parameter is plotted in red and the median is plotted in black. The interquartile range is shaded in gray.

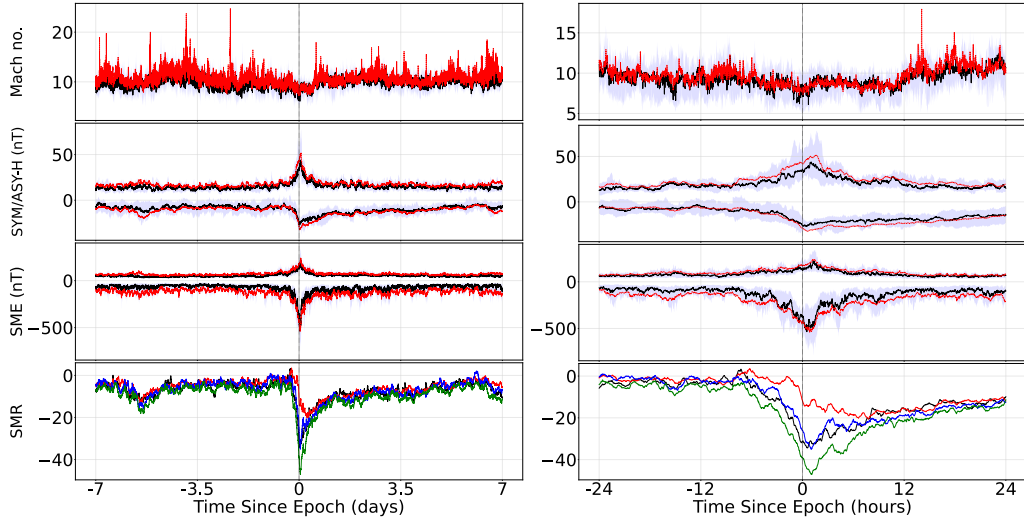


Figure 3. Two week (left) and two day (right) superposed epoch analyses of solar wind Alfvén Mach number, SYM-H, ASY-H, SML, SMU, and local ring current indices (SMR) measured during the 28 omega band events. The epoch time is defined as the minute that the omega bands were observed. SYM-H/ASY-H and SML/SMU are overplotted. In the top three panels, the mean value of each parameter is plotted in red, the median is plotted in black, and the interquartile range is shaded in gray. In the lower panel, SMR00 is plotted in black, SMR06 is plotted in red, SMR12 is plotted in blue, and SMR18 is plotted in green.

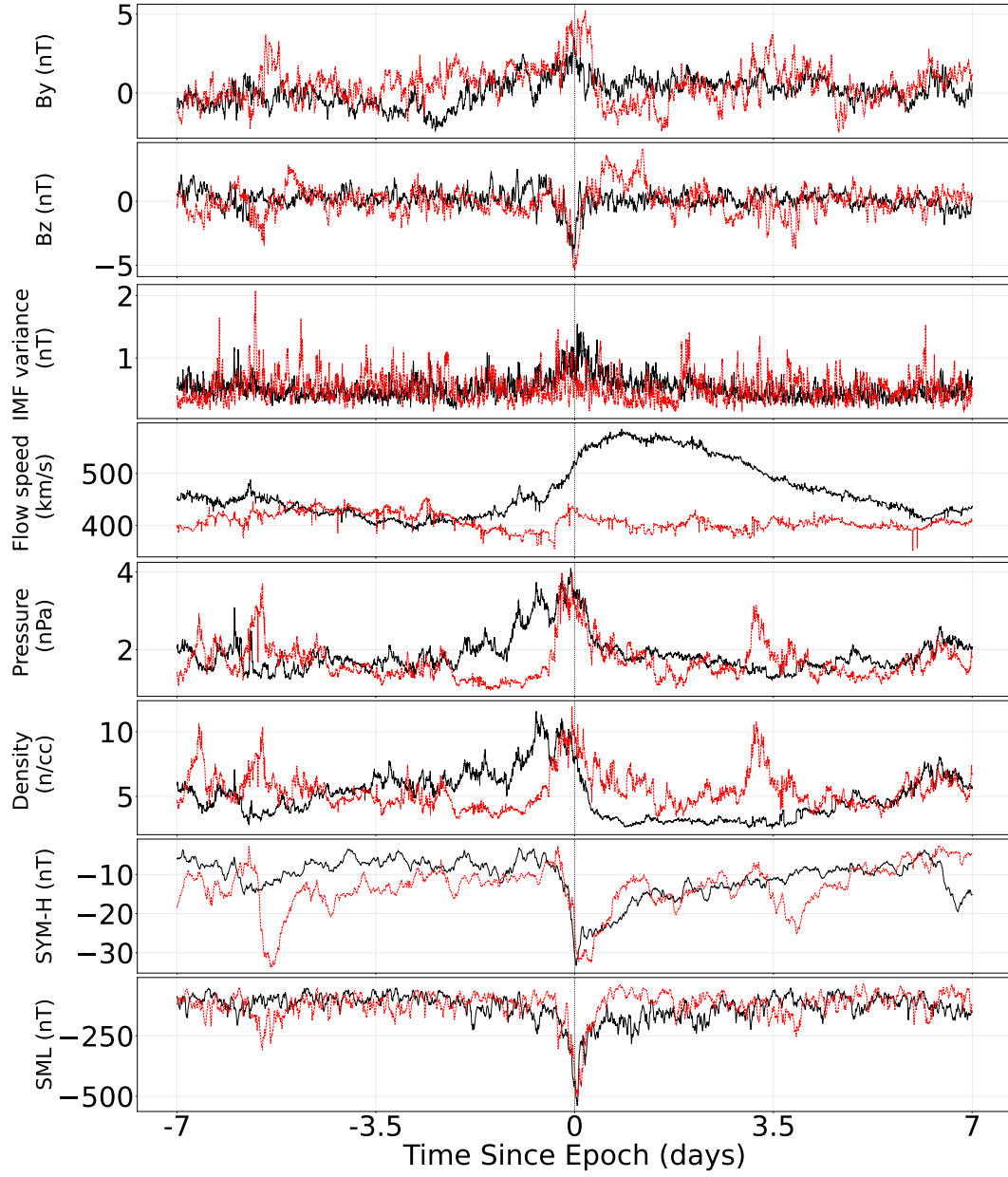


Figure 4. Two week superposed epoch analyses of IMF B_y , IMF B_z , IMF vector variance, solar wind flow speed, solar wind pressure, solar wind proton density, SYM-H, and SML measured in GSM coordinates during SIR and non-SIR events. The epoch time is defined as the minute that the omega bands were observed. The mean values of each parameter for the SIR events are plotted in black and the mean values for the non-SIR events are plotted in red. 15-minute rolling averages of each parameter are shown here.